Pyrite sulfur isotopes reveal glacial–interglacial environmental changes

Virgil Pasquier[a,1], Pierre Sansjofre[a], Marina Rabineau[a], Sidonie Revillon[a,b], Jennifer Houghton[c], and David A. Fike[c]

[a]Laboratoire Géosciences Océan, UMR CNRS-6538, Institut Universitaire Européen de la Mer, Université Bretagne Occidentale, 29280 Plouzane, France; [b]SEDISOR, Institut Universitaire Européen de la Mer, 29280 Plouzane, France; and [c]Department of Earth and Planetary Sciences, Washington University in St. Louis, St. Louis, MO 63130

Edited by John P. Grotzinger, California Institute of Technology, Pasadena, CA, and approved April 12, 2017 (received for review November 3, 2016)

The sulfur biogeochemical cycle plays a key role in regulating Earth's surface redox through diverse abiotic and biological reactions that have distinctive stable isotopic fractionations. As such, variations in the sulfur isotopic composition ($\delta^{34}S$) of sedimentary sulfate and sulfide phases over Earth history can be used to infer substantive changes to the Earth's surface environment, including the rise of atmospheric oxygen. Such inferences assume that individual $\delta^{34}S$ records reflect temporal changes in the global sulfur cycle; this assumption may be well grounded for sulfate-bearing minerals but is less well established for pyrite-based records. Here, we investigate alternative controls on the sedimentary sulfur isotopic composition of marine pyrite by examining a 300-m drill core of Mediterranean sediments deposited over the past 500,000 y and spanning the last five glacial–interglacial periods. Because this interval is far shorter than the residence time of marine sulfate, any change in the sulfur isotopic record preserved in pyrite ($\delta^{34}S_{pyr}$) necessarily corresponds to local environmental changes. The stratigraphic variations (>76‰) in the isotopic data reported here are among the largest ever observed in pyrite, and are in phase with glacial–interglacial sea level and temperature changes. In this case, the dominant control appears to be glacial–interglacial variations in sedimentation rates. These results suggest that there exist important but previously overlooked depositional controls on sedimentary sulfur isotope records, especially associated with intervals of substantial sea level change. This work provides an important perspective on the origin of variability in such records and suggests meaningful paleoenvironmental information can be derived from pyrite $\delta^{34}S$ records.

pyrite sulfur isotopes | glacial | interglacial | sedimentation rate | local environment changes

The sulfur biogeochemical cycle helps regulate Earth's surface redox conditions through a variety of abiotic and biological reactions (1). These diverse reactions are often associated with distinctive stable isotopic fractionations of sulfur species (2, 3). As such, changes in the sulfur isotopic composition ($\delta^{34}S$) of sedimentary phases over Earth history are often used to infer substantive changes to Earth's surface environment, including the rise of atmospheric oxygen, the oxygenation of the oceans, and episodes of metazoan evolution and mass extinction (2–6). Much of past efforts to reconstruct the ancient sulfur cycle has used sulfate evaporite minerals (gypsum and anhydrite), barium sulfate (barite), or carbonate-associated sulfate [i.e., sulfate bound into carbonate lattice, carbonate-associated sulfate (CAS)], all proxies commonly used to accurately reflect the $\delta^{34}S$ composition of seawater sulfate (2, 7). Additional constraints on ancient biogeochemical cycling have been placed through the analysis of $\delta^{34}S$ records from sedimentary pyrites, either in parallel with direct proxies for sulfate (4, 6, 8, 9), or on their own (10–13). Inferences about past biogeochemical cycling are based on the assumption that the $\delta^{34}S$ records reflect the isotopic composition of seawater sulfate and, further, that changes in these values indicate large-scale temporal changes in the global sulfur cycle. However, a subset of records of sulfur cycling from certain intervals on Earth have shown substantial spatial and stratigraphic variability that is not easily reconciled with them reflecting the behavior of the global sulfur cycle (e.g., ref. 14). Rather, it has been suggested that some $\delta^{34}S$ records have the potential to be impacted by local depositional conditions (2), and, further, that these records may provide new insights into paleo-environmental conditions. This intriguing idea has, however, not yet been appropriately tested.

Here we examine the sulfur isotopic record preserved in pyrite ($\delta^{34}S_{pyr}$) from sediments from the Gulf of Lion deposited over the last 500,000 y associated with the last five glacial–interglacial transitions. Gulf of Lion is located in the northwestern Mediterranean basin and is characterized by a wide continental shelf (70 km) that was subaerially exposed during glacial periods over the Late Quaternary (15, 16). This study is based on borehole PRGL1-4 (Fig. 1), drilled in the framework of the European Union Profiles Across Mediterranean Sedimentary Systems (PROMESS) project (https://www.pangaea.de/?q=PROMESS1), which sampled a 300-m-long continuous record of the Bourcart and Herault canyons' interfluve sediment sequence on the upper slope of the Gulf of Lion (Fig. 1). The water depth of the core (298 m) ensures continued deposition under well-oxygenated conditions during glacial and interglacial periods with sedimentation rates that enable high-resolution records and where the changing proximity to the continental shelf results in variable detrital input. Given these characteristics, this drill core represents a record of glacial–interglacial deposition that is uniquely positioned to assess the environmental dependence of $\delta^{34}S_{pyr}$ signatures in marine sediments.

Significance

Changes in sulfur isotope ratios ($^{34}S/^{32}S$) of marine sulfur phases are often attributed to global biogeochemical perturbations. Sediments collected on the shelf of the Gulf of Lion revealed remarkable sulfur isotopic fluctuations in sedimentary pyrite over the last 500,000 years, ranging between −44.0‰ and 32.3‰. We suggest this pattern is related to changes in the local environmental deposition, specifically, sedimentation modulating connectivity with the overlying water column and resulting microbial activity. Besides providing new understanding of an important and poorly constrained aspect of past glacial–interglacial transitions, our results are critically important because they question the degree to which changes in sulfur isotopes in pyrite reflect global biogeochemical processes versus local depositional conditions.

Author contributions: P.S., M.R., S.R., and D.A.F. designed research; V.P., P.S., and D.A.F. performed research; V.P. and J.H. contributed new reagents/analytic tools; V.P., P.S., and D.A.F. analyzed data; and V.P., P.S., M.R., S.R., J.H., and D.A.F. wrote the paper.

The authors declare no conflict of interest.

This article is a PNAS Direct Submission.

[1]To whom correspondence should be addressed. Email: virgil.pasquier@univ-brest.fr.

This article contains supporting information online at www.pnas.org/lookup/suppl/doi:10.1073/pnas.1618245114/-/DCSupplemental.

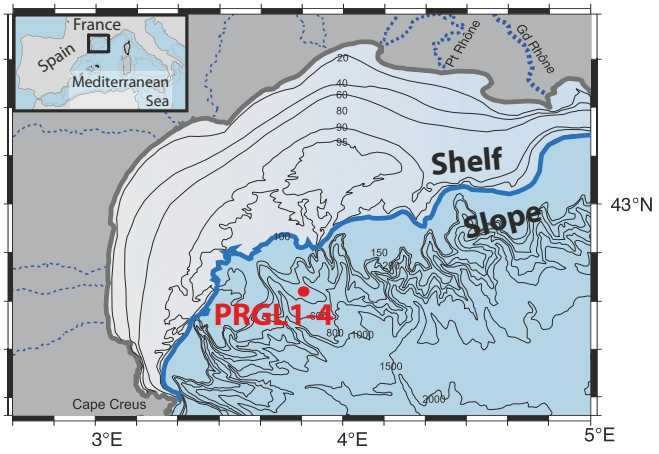

Fig. 1. Map of the Gulf of Lion with the position of the PRGL1-4 core (42.690°N, 3.838°E). The bold gray line highlights the present shoreline position, and the contours reflect modern water depths. The bold blue line corresponds to the shoreline position during the last glacial period (low sea level).

Results and Discussion

A total of 131 pyrite sulfur isotopes analyses have been performed along the 300-m PRGL1-4 core, spanning the last five glacial–interglacial transitions (Fig. S1 and Table S1). Throughout the core, pyrite shows extreme variations in $\delta^{34}S$, from −44.0‰ to 32.3‰, whereas pyrite contents vary between 0.02 wt % and 1.69 wt %. No clear trend was observed between $\delta^{34}S_{pyr}$ and the pyrite content, nor between $\delta^{34}S_{pyr}$ and the iron content (Figs. S1 and S2). Complementary analysis of organic carbon isotopes ($\delta^{13}C_{org}$) was conducted, and these values vary between −25.3‰ and −21.8‰, with no clear trends between $\delta^{13}C_{org}$ and total organic carbon (TOC) contents, which vary between 0.35% and 0.84%. Similarly, we do not observe any covariation between $\delta^{34}S_{pyr}$ and TOC (Figs. S1 and S2).

A clear distinction in pyrite $\delta^{34}S_{pyr}$ values is observed between glacial and interglacial periods (Fig. 2) as deduced from the oxygen isotope curve obtained from planktonic foraminifera (*Globigerina bulloides*) and the associated updated age model published on the same core (17). Distinctly different bimodal distributions are observed between glacial (*sensu stricto,* i.e., cold substages) periods with high $\delta^{34}S$ values and high isotopic variability (average $\delta^{34}S = -15.2‰ \pm 9.0‰$, $n = 46$) and the interglacial (*sensu stricto,* i.e., warm substages) periods characterized by low $\delta^{34}S$ and low isotopic variability (average $\delta^{34}S = -41.6‰ \pm 2.2‰$, $n = 19$; Fig. 2). The increased variability observed during glacial times provides insights into the suite of processes and their inherent temporal fluctuations that are likely to regulate the observed changes in $\delta^{34}S_{pyr}$. Specifically, the lowered sea level during glacial times brought the site of deposition closer to the shore and source of detrital materials. These shallower, more proximal settings are subjected to short-term, stochastic variations in depositional conditions (17), including sediment characteristics (organic carbon loading, sedimentation rates, physical reworking) and benthic ecology (bioturbation, presence of microbial mats) that can impact pyrite formation and eventual $\delta^{34}S$ composition. Within the glacial and interglacial sediments, the $\delta^{34}S$ values and variability can be further understood as a function of temperature, as reconstructed from alkenone records (18, 19). For example, warmer intervals during interglacial time are associated with more negative $\delta^{34}S$ values (Fig. 2).

Over the last two glacial–interglacial cycles, where the time reconstruction is best constrained, pyrite $\delta^{34}S$ values in PRGL1-4 are modulated by and track depositional conditions across glacial–interglacial cycles (Fig. 3). During glacial times, higher $\delta^{34}S_{pyr}$ values are associated with lower sea levels and low $\delta^{13}C_{org}$ values, which are often attributed to greater input of terrestrial organic matter (20). Interestingly, because of their increased proximity to shore, glacial deposits are also associated with increased sedimentation rates of silty clay sediments (21) and are characterized by decreased porosity intervals (Fig. S3). In such nearshore environments, the rapid sediment burial dilutes TOC values. Nevertheless, a higher concentration of labile organic matter (supported by our TOC values) gets into the sediment without undergoing aerobic respiration. As such, a larger fraction of more easily metabolizable (i.e., less degraded by oxic processes) organic matter is available for sulfate reduction during glacial intervals (22).

In contrast, decreased and less variable $\delta^{34}S_{pyr}$ values are associated with the transition into and during interglacial times. These periods are associated with warmer temperatures and higher sea levels, as well as increased $\delta^{13}C_{org}$ values, indicative of increased marine input (23). Sediments deposited during interglacial periods are also associated with lower sedimentation rates (because of landward migration of the shoreline) and increased foraminiferal abundance, resulting in intervals of higher porosity (21) (Fig. S3). As sedimentation rates decrease, organic matter spends more time in the zone of aerobic respiration. Therefore, less (and less reactive) organic matter remains for sulfate-reducing bacteria under these conditions.

Stratigraphic variations in pyrite $\delta^{34}S$ are often interpreted to reflect changes in the global sulfur biogeochemical cycle, such as intervals of enhanced pyrite burial or variations in the marine sulfate reservoir (9, 24). However, in this case, these strata were deposited over an interval of 500 ky, much less than the residence

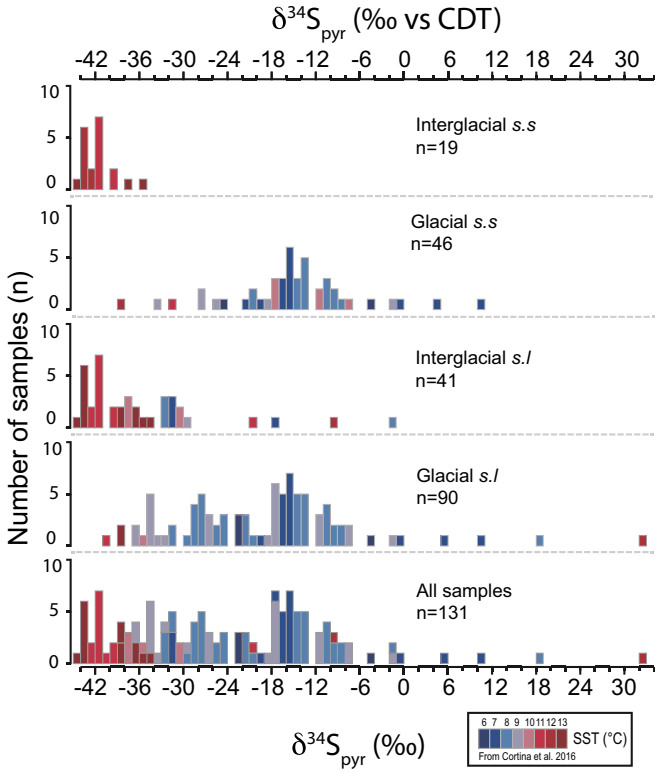

Fig. 2. Histogram of pyrite $\delta^{34}S$ (this study) as a function of glacial/interglacial periods, color-coded by temperature obtained from the relative composition of C_{37} unsaturated alkenones (18, 19). *Sensu stricto* (*s.s.*) refers to the warm substages of the interglacials and cold substages during glacials. The *sensu latto* (*s.l.*) includes all of the data within interglacial or glacial periods.

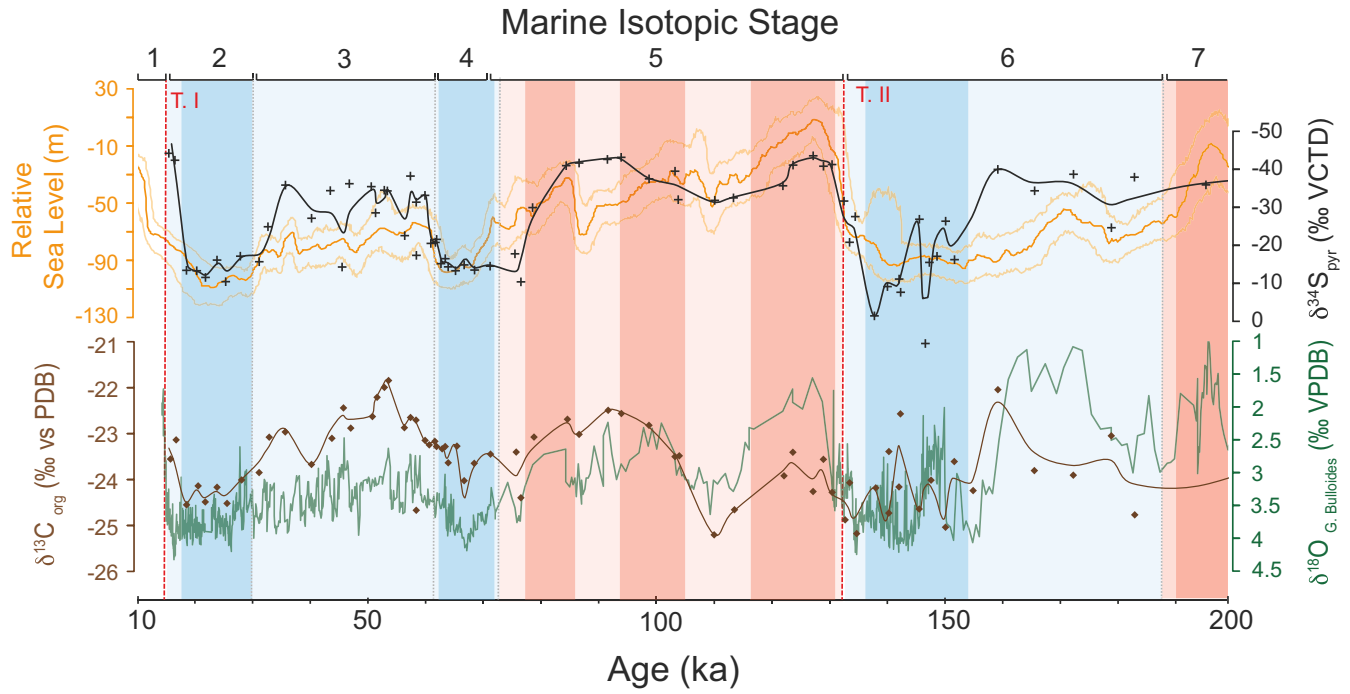

Fig. 3. Glacial–interglacial geochemical records. Shown are the $\delta^{34}S_{pyr}$ (black crosses; black line representing LOESS regression, this study), $\delta^{13}C_{org}$ (brown diamonds and brown line (local polynomial regression type LOESS, this study), reconstructed sea levels (orange) from the Red Sea, and $\delta^{18}O_{G.\ Bulloides}$ (green) for the last six Marine isotopic stages (10 ky to 200 ky). Also shown are relative sea level (orange line) superimposed with 95% of probability interval (light orange lines) from ref. 43 and $\delta^{18}O_{G.Bulloides}$ from refs. 17 and 21. Blue vertical bands represent the glacial times, with corresponding cold substages (i.e., *sensu stricto*) in darker blue. Red bands correspond to interglacial periods, with warm substages (i.e., *sensu stricto*) highlighted in dark pink. Vertical red dashed lines reflect glacial termination (T.) times are according to ref. 44; vertical gray dashed lines reflect scheme of marine stages according to ref. 45.

time [13 My (25)] of sulfate in the modern ocean. While these sediments were deposited in the Gulf of Lion, the Mediterranean Sea maintained connectivity with the global ocean and retained marine sulfate abundances and isotopic compositions during glacial–interglacial periods, based on both the abundance and isotopic composition of sulfate pore water profiles (26) and the continuous sea water infill of Mediterranean Sea by Atlantic water through the Gilbraltar Strait since ∼4.4 Ma (27, 28). Thus, continued connectivity with the ocean and the short timescale of deposition preclude any substantive change in the parent sulfate reservoir, such as might arise from prolonged variation in the burial flux of pyrite, during deposition of these sediments. How then is this variation in pyrite $\delta^{34}S$ to be interpreted?

Mechanistic Explanations. Two possible mechanisms present themselves to explain the observed data—both fundamentally driven by glaciation induced environmental changes: one reflecting changes in the inherent metabolic activity of sulfur cycling microbes in the sediments, and the other reflecting changes in the connectivity of pore waters to the overlying water column. In the former, isotopic fractionation during microbial sulfur cycling is typically dominated by microbial sulfate reduction (3), and a change in pyrite $\delta^{34}S$ can result from variations in the rate of cell-specific sulfate reduction (csSRR) in these sediments (29). Specifically, there is a well-documented relationship whereby faster rates of csSRR are associated with decreased isotopic fractionation between the parent sulfate and the produced sulfide (29, 30). Thus, our data could indicate faster csSRR during glacial times, possibly driven by enhanced input of more easily metabolizable organic matter [as supported by lower organic carbon isotopic values (Fig. S1)]. In contrast, slower csSRR would characterize interglacial times associated with more stable and more limited (both in abundance and reactivity) organic matter resources.

Assuming that pyrite is formed mainly in the pore water environment, as is expected under an oxygenated (noneuxinic) water column (31), an alternative mechanism to explain our data involves a change in the connectivity of sedimentary pore waters where pyrites are forming with the overlying water column (32). Such a change could be the natural result of the increased sedimentation rates and decreased porosity during glacial times (Fig. S3), both of which act to more effectively isolate pore waters from ready communication with seawater. This decreased connectivity effectively isolates the local pore water sulfate reservoir, leading to increased pore water $\delta^{34}S_{SO4}$ through ongoing microbial sulfate reduction (32). In turn, this microbial activity naturally leads to an increase in the resulting biogenic $\delta^{34}S_{H2S}$, which eventually forms pyrite following reaction with available iron. The increased variability in $\delta^{34}S_{pyr}$ during glacial times can be understood as the natural response to increased short-term fluctuations in depositional conditions that characterize shallower water environments more proximal to the shore. During interglacial times, the return to slower sedimentation rates and higher porosity, driven in part by the admixture of foraminifera (Fig. S3), results in enhanced communication between pore water and seawater. In this relatively open system, the constant supply of seawater sulfate results in a stable, low value for pore water $\delta^{34}S_{SO4}$ (and therefore in the resulting $\delta^{34}S_{pyr}$) in these intervals. Although the relationship between sedimentation rate and $\delta^{34}S_{pyr}$ indicates a dominant control by sedimentation (Fig. 4), it should be noted that these two mechanisms are not mutually exclusive. Indeed, all things being equal, increased csSRR will inherently lead to more closed system behavior because it represents enhanced sulfate consumption relative to the diffusive exchange of sulfate. Further, there is a general trend toward increasing rates of sulfate reduction with increasing sedimentation rate (33).

The magnitude and directionality of the relationship between water depth and pyrite $\delta^{34}S$ observed here agree with predictions previously made (2) but never rigorously tested and provide a powerful

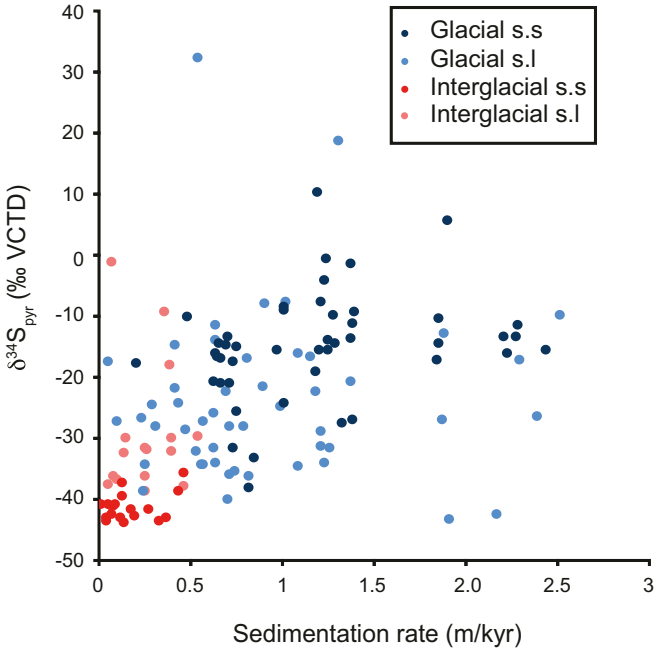

Fig. 4. The relationship between sedimentation rate (meters per kiloyear) and $\delta^{34}S_{pyr}$. Sedimentation rates are calculated using the linear relationship between depth in borehole and the update age model derived from ref. 17. Light/dark blues circles correspond to cold substages (i.e., respectively *sensu lato* and *sensu stricto*), and light/dark red circles refer to warm substages (i.e., respectively *sensu lato* and *sensu stricto).*

way to reconstruct paleoenvironmental conditions in sedimentary environments, particularly the degree to which sedimentary pore fluids may have been in communication with the overlying water column. In addition, the $\delta^{34}S_{pyr}$ data presented here also shed light on the possible origins of similar variability in this proxy in deep time.

Implication for Deep-Time Records. Many deep-time studies make use of direct proxies for seawater sulfate, such as CAS, which are generally thought to reflect marine sulfate with little fractionation (e.g., ref. 7; but see ref. 34). Indeed, studies using direct proxies for seawater sulfate (e.g., refs. 9, 24, 35, and 36) can provide powerful insights into ancient biogeochemical conditions. In many cases, however, no direct proxy of seawater sulfate is present and stratigraphic records of $\delta^{34}S_{pyr}$ are used to reconstruct global biogeochemical cycling and redox change (e.g., refs. 10–13). In other cases, the isotopic offsets between coeval $\delta^{34}S$ records from sulfate and pyrite are used to reconstruct marine sulfate levels or the types of microbial metabolism present (e.g., refs. 4 and 8). With few exceptions (e.g., ref. 6), these $\delta^{34}S_{pyr}$ records are not interpreted in the context of local depositional or facies change.

Interestingly, many of the reports showing positive $\delta^{34}S_{pyr}$ excursions in the rock record are also associated with shallowing-upward depositional sequences formed during sea level lowstands. The present study is particularly relevant for considering the ∼10 to 30‰ positive excursions in $\delta^{34}S_{pyr}$ that are associated with the initiation and termination of the end-Ordovician Hirnantian glaciation and mass extinction (e.g., refs. 6 and 10–13). Depositional environments at this time experienced a magnitude (∼100 m) and timescale ($\sim10^5$ y) of sea level change that would have been comparable to those influencing the Pleistocene sediments of the Gulf of Lion. Our data suggest that, rather than reflecting a change in the global sulfur cycle, these $\delta^{34}S_{pyr}$ excursions could also be explained by local changes in depositional conditions, particularly changes in sedimentation that modulate connectivity with the overlying water column (e.g., Fig. 4). In this scenario, it is local sedimentological changes that impact how records of sulfur cycling get preserved in sedimentary records. The temporal coincidence of the Hirnantian $\delta^{34}S_{pyr}$ excursions, found in sections around the world associated with the end Ordovician glaciation, would then be the result of synchronous local changes in environmental conditions in basins around the world, changes driven globally by sea level fluctuations during the onset and termination of the Hirnantian glaciation. Local environmental controls could be relevant for explaining other stratigraphic $\delta^{34}S_{pyr}$ excursions in Earth history, particularly those associated with changing depositional facies and lacking a direct proxy for the marine sulfate reservoir (e.g., refs. 37–39). As such, the data presented here show that pyrite $\delta^{34}S$ can be a valuable proxy for reconstructing local paleoenvironmental and sedimentological conditions throughout Earth history.

Materials and Methods

Pyrite Sulfur ($\delta^{34}S_{pyrite}$ and S Content). Pyrite sulfur from the samples was extracted using the chromium reduction method (40–42). This method allows a recovering of all reduced inorganic sulfur present in sedimentary samples (pyrite, element sulfur, and iron monosulfide phases). During extraction, samples were reacted with ∼25 mL of 1 M reduced chromium chloride ($CrCl_2$) solution and 25 mL of 6N HCl for 4 h in a specialized extraction line under a Nitrogen atmosphere. The liberated hydrogen sulfide was reacted in a silver nitrate (0.1 M) trap, recovering the sulfide as Ag_2S; reproducibility was under 5% for repeated analyze. Residual Ag_2S were rinsed three times using Mili-Q water, centrifuged, and then the dried until complete dryness. The Ag_2S powders were homogenized before being analyzed; then 450 μg was loaded into tin capsules with excess V_2O_5. The Ag_2S was analyzed measuring $^{34}S/^{32}S$ ratio following online combustion with a Thermo Delta V Plus coupled with a Costech ECS 4010 Elemental Analyzer at Washington University in St. Louis. Pyrite sulfur composition are expressed in standard delta notation as per mil (‰) deviations from Vienna Canyon Diablo Troilite with an analytical error of <0.5‰.

Organic Carbon Analyses ($\delta^{13}C_{org}$ and TOC). Before organic carbon and nitrogen analyses, the carbonated fraction was removed from bulk samples using excess 1.5 HCl digestion for 48 h. During digestion, centrifuge tubes were placed in an ultrasonic bath to increase the mechanical separation of clay and calcium carbonates. After total dissolution, residues were washed three times with distilled water, centrifuged, and then dried at 50 °C. The residual powders were homogenized, and, before analyses, 30 mg were loaded into a tin capsule. Analyses were performed using an Elemental Analyzer (EA, Flash 2000; Thermo Scientific) coupled to an isotope ratio mass spectrometer (Delta V+ Thermo Scientific EA-IRMS) at the Pôle de Spectométrie Océan (PSO). Carbon is given as delta notation as per mil deviation from Pee Dee Belemnite, with an analytical error of <0.2‰ (1σ) for organic carbon isotopes. TOC was measured using the Thermal Conductivity Detector of the Flash EA 2000 (Thermo Scientific) at PSO.

ACKNOWLEDGMENTS. We thank the European PROMESS Scientific committee and colleagues at Ifremer for previous contributions of data acquisition, processing, interpretations, and permission to resample the borehole. We acknowledge C. Liorzou, who kindly helped during the analytical preparation of samples, and O. Lebeau, for stable isotope analyses assistance in Brest. This work was supported by the "Laboratoire d'Excellence" LabexMER (Grant ANR-10-LABX-19) and was cofunded by a grant from the French government under the program "Investissements d'Avenir," and by a grant from the Regional Council of Brittany. Additional founding came from Actions Marges Program (Mediterranean Sea). The drilling operation was conducted within the European Commission Project PROMESS (Contract EVR1-CT-2002-40024).

1. Garrels RM, Lerman A (1981) Phanerozoic cycles of sedimentary carbon and sulfur. *Proc Natl Acad Sci USA* 78:4652–4656.
2. Fike DA, Bradley AS, Rose CV (2015) Rethinking the ancient sulfur cycle. *Annu Rev Earth Planet Sci* 43:593–622.
3. Canfield DE (2001) Biogeochemistry of sulfur isotopes. *Rev Mineral Geochem* 43: 607–636.
4. Fike DA, Grotzinger JP, Pratt LM, Summons RE (2006) Oxidation of the Ediacaran ocean. *Nature* 444:744–747.
5. Riccardi AL, Arthur MA, Kump LR (2006) Sulfur isotopic evidence for chemocline upward excursions during the end-Permian mass extinction. *Geochim Cosmochim Acta* 70:5740–5752.
6. Jones DS, Fike DA (2013) Dynamic sulfur and carbon cycling through the end-Ordovician extinction revealed by paired sulfate–pyrite δ 34 S. *Earth Planet Sci Lett* 363:144–155.

7. Kampschulte A, Strauss H (2004) The sulfur isotopic evolution of Phanerozoic seawater based on the analysis of structurally substituted sulfate in carbonates. *Chem Geol* 204:255–286.
8. Hurtgen MT, Halverson GP, Arthur MA (2006) Sulfur cycling in the aftermath of a 635-Ma snowball glaciation: Evidence for a syn-glacial sulfidic deep ocean. *Earth Planet Sci Lett* 245:551–570.
9. Gill BC, et al. (2011) Geochemical evidence for widespread euxinia in the later Cambrian ocean. *Nature* 469:80–83.
10. Yan D, Chen D, Wang Q, Wang J, Wang Z (2009) Carbon and sulfur isotopic anomalies across the Ordovician–Silurian boundary on the Yangtze Platform, South China. *Palaeogeogr Palaeoclimatol Palaeoecol* 274:32–39.
11. Zhang T, Shen Y, Zhan R, Shen S, Chen X (2009) Large perturbations of the carbon and sulfur cycle associated with the Late Ordovician mass extinction in South China. *Geology* 37:299–302.
12. Gorjan P, Kaiho K, Fike DA, Xu C (2012) Carbon-and sulfur-isotope geochemistry of the Hirnantian (Late Ordovician) Wangjiawan (Riverside) section, South China: Global correlation and environmental event interpretation. *Palaeogeogr Palaeoclimatol Palaeoecol* 337-338:14–22.
13. Hammarlund EU, Dahl TW, Harper D (2012) A sulfidic driver for the end-Ordovician mass extinction. *Earth Planet Sci Lett* 331-332:128–139.
14. Ries JB, Fike DA, Pratt LM, Lyons TW (2009) Superheavy pyrite ($\delta^{34}S_{pyr} > \delta^{34}S_{CAS}$) in the terminal Proterozoic Nama Group, southern Namibia: A consequence of low seawater sulfate at the dawn of animal life. *Geology* 37:743–746.
15. Rabineau M, Berné S, Aslanian D, Olivet JL (2005) Sedimentary sequences in the Gulf of Lion: A record of 100,000 years climatic cycles. *Mar Pet Geol* 22:775–804.
16. Jouet G, Berné S, Rabineau M, Bassetti MA, Bernier P (2006) Shoreface migrations at the shelf edge and sea-level changes around the Last Glacial Maximum (Gulf of Lions, NW Mediterranean). *Mar Geol* 234:21–42.
17. Cortina A, Sierro FJ, Gonzalez-Mora B, Asioli A (2011) Impact of climate and sea level changes on the ventilation of intermediate water and benthic foraminifer assemblages in the Gulf of Lions, off South France, during MIS 11 in the northwestern Mediterranean Sea (Gulf of Lions). *Palaeogeogr Palaeoclimatol Palaeoecol* 309: 215–228.
18. Cortina A, Sierro FJ, Flores JA (2015) The response of SST to insolation and ice sheet variability from MIS 3 to MIS 11 in the northwestern Mediterranean Sea (Gulf of Lions). *Geophys Res Lett* 42:10366–10374.
19. Cortina A, Grimalt JO, Martrat B (2016) Anomalous SST warming during MIS 13 in the Gulf of Lions (northwestern Mediterranean Sea). *Org Geochem* 92:16–23.
20. Lamb AL, Wilson GP, Leng MJ (2006) A review of coastal palaeoclimate and relative sea-level reconstructions using $\delta^{13}C$ and C/N ratios in organic material. *Earth Sci Rev* 75:29–57.
21. Sierro FJ, Andersen N, Bassetti MA, Berné S (2009) Phase relationship between sea level and abrupt climate change. *Quat Sci Rev* 28:2867–2881.
22. Canfield DE (1989) Sulfate reduction and oxic respiration in marine sediments: Implications for organic carbon preservation in euxinic environments. *Deep Sea Res A* 36:121–138.
23. Tesi T, Miserocchi S, Goñi MA, Langone L (2007) Source, transport and fate of terrestrial organic carbon on the western Mediterranean Sea, Gulf of Lions, France. *Mar Chem* 105:101–117.
24. Owens JD, Gill BC, Jenkyns HC (2013) Sulfur isotopes track the global extent and dynamics of euxinia during Cretaceous Oceanic Anoxic Event 2. *Proc Natl Acad Sci USA* 110:18407–18412.
25. Kah LC, Lyons TW, Frank TD (2004) Low marine sulphate and protracted oxygenation of the Proterozoic biosphere. *Nature* 431:834–838.
26. Böttcher ME, Bernasconi SM, Brumsack H-J (1999) Carbon, sulfur, and oxygen isotope geochemistry of interstitial waters from the Western Mediterranean. *Proc Ocean Drill Program Sci Results* 161:413–421.
27. Rohling EJ, et al. (2014) Sea-level and deep-sea-temperature variability over the past 5.3 million years. *Nature* 508:477–482.
28. Hernández-Molina FJ, et al. (2014) Onset of Mediterranean outflow into the North Atlantic. *Science* 344:1244–1250.
29. Sim MS, Ono S, Donovan K, Templer SP (2011) Effect of electron donors on the fractionation of sulfur isotopes by a marine *Desulfovibrio* sp. *Geochim Cosmochim Acta* 75:4244–4259.
30. Leavitt WD, Halevy I, Bradley AS (2013) Influence of sulfate reduction rates on the Phanerozoic sulfur isotope record. *Proc Natl Acad Sci USA* 110:11244–11249.
31. Censi P, Incarbona A, Oliveri E, Bonomo S, Tranchida G (2010) Yttrium and REE signature recognized in Central Mediterranean Sea (ODP Site 963) during the MIS 6–MIS 5 transition. *Palaeogeogr Palaeoclimatol Palaeoecol* 292:201–210.
32. Gomes ML, Hurtgen MT (2013) Sulfur isotope systematics of a euxinic, low-sulfate lake: Evaluating the importance of the reservoir effect in modern and ancient oceans. *Geology* 41:663–666.
33. Claypool GE (2004) Ventilation of marine sediments indicated by depth profiles of pore water sulfate and $\delta^{34}S$. *Spec Publ Geochem Soc* 9:59–65.
34. Present TM, Paris G, Burke A, Fischer W (2015) Large carbonate associated sulfate isotopic variability between brachiopods, micrite, and other sedimentary components in Late Ordovician strata. *Earth Planet Sci Lett* 432:187–198.
35. Fike DA, Grotzinger JP (2008) A paired sulfate–pyrite $\delta^{34}S$ approach to understanding the evolution of the Ediacaran–Cambrian sulfur cycle. *Geochim Cosmochim Acta* 72: 2636–2648.
36. Sansjofre P, et al. (2016) Multiple sulfur isotope evidence for massive oceanic sulfate depletion in the aftermath of Snowball Earth. *Nat Commun* 7:12192.
37. Goldberg T, Strauss H, Guo Q, Liu C (2007) Reconstructing marine redox conditions for the Early Cambrian Yangtze Platform: Evidence from biogenic sulphur and organic carbon isotopes. *Palaeogeogr Palaeoclimatol Palaeoecol* 254:175–193.
38. Feng LJ, Chu XL, Huang J, Zhang QR, Chang HJ (2010) Reconstruction of paleo-redox conditions and early sulfur cycling during deposition of the Cryogenian Datangpo Formation in South China. *Gondwana Res* 18:632–637.
39. Parnell J, Boyce AJ, Mark D, Bowden S, Spinks S (2010) Early oxygenation of the terrestrial environment during the Mesoproterozoic. *Nature* 468:290–293.
40. Canfield DE, Raiswell R, Westrich JT, Reaves CM (1986) The use of chromium reduction in the analysis of reduced inorganic sulfur in sediments and shales. *Chem Geol* 54: 149–155.
41. Tuttle ML, Goldhaber MB, Williamson DL (1986) An analytical scheme for determining forms of sulphur in oil shales and associated rocks. *Talanta* 33:953–961.
42. Burton ED, Sullivan LA, Bush RT, Johnston SG (2008) A simple and inexpensive chromium-reducible sulfur method for acid-sulfate soils. *Appl Geochem* 23:2759–2766.
43. Grant KM, et al. (2014) Sea-level variability over five glacial cycles. *Nat Commun* 5:5076.
44. Barker S, et al. (2011) 800,000 years of abrupt climate variability. *Science* 334:347–351.
45. Railsback LB, Gibbard PL, Head MJ (2015) An optimized scheme of lettered marine isotope substages for the last 1.0 million years, and the climatostratigraphic nature of isotope stages and substages. *Quat Sci Rev* 111:94–106.

Supporting Information

Pasquier et al. 10.1073/pnas.1618245114

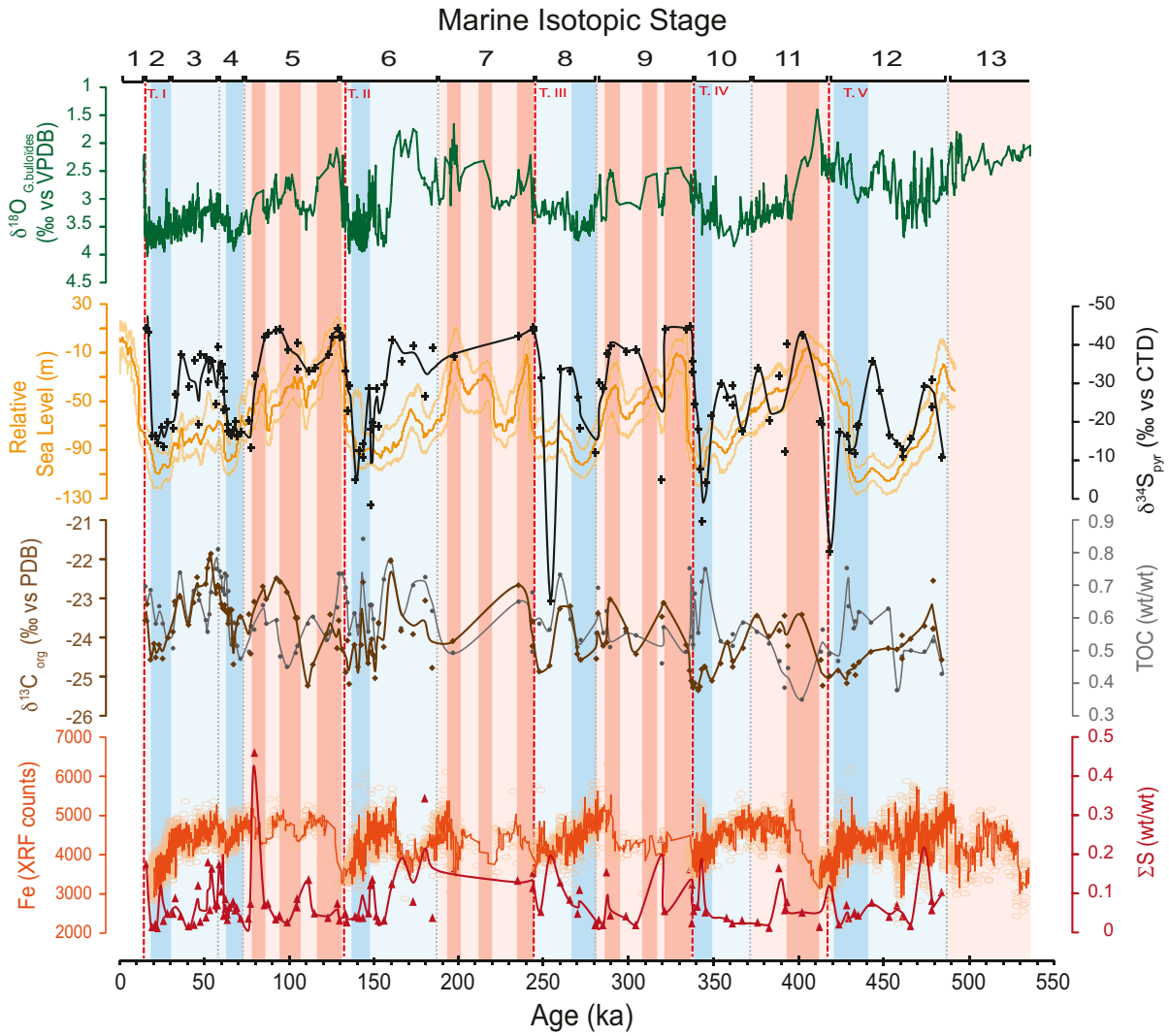

Fig. S1. The $\delta^{18}0_{G.bulloïdes}$ (green line from refs. 17 and 21) and $\delta^{34}S_{pyr}$ (black crosses and the black line represent local polynomial regression type LOESS between measured points, this study) associated with relative sea level (orange line) superimposed with 95% of probability interval (light orange lines) from ref. 43. Also shown are the $\delta^{13}C_{org}$ [brown diamonds and line (LOESS regression), this study] and associated TOC [gray line (LOESS regression) associated with gray circles]. Iron record from X-ray fluorescence core scanning (orange line) and total sulfide (TS, red line, this study) also are given. Blue bands represent the glacial times, with corresponding cold substages (i.e., *sensu stricto*) in darker blue. Red bands correspond to interglacial periods, with warm substages (i.e., *sensu stricto*) highlighted in dark pink. Termination (T.) is according to ref. 44. Scheme of marine stage is according to ref. 45.

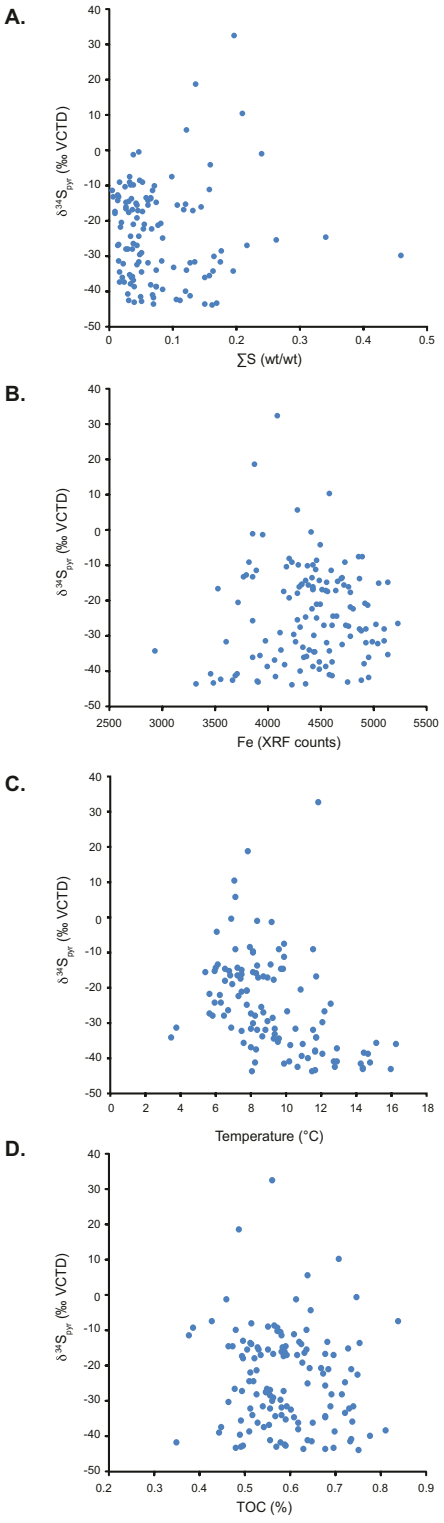

Fig. S2. (*A*) Cross-plot between $\delta^{34}S_{pyr}$ with associated total sulfur species present in sediment (TS wt %); (*B*) $\delta^{34}S_{pyr}$ with Fe_{XRF_counts}; (*C*) $\delta^{34}S_{pyr}$ against temperature obtained from the relative composition of C_{37} unsaturated alkenones from refs. 18 and 19; and (*D*) $\delta^{34}S_{pyr}$ with TOC within sediment (TOC wt %).

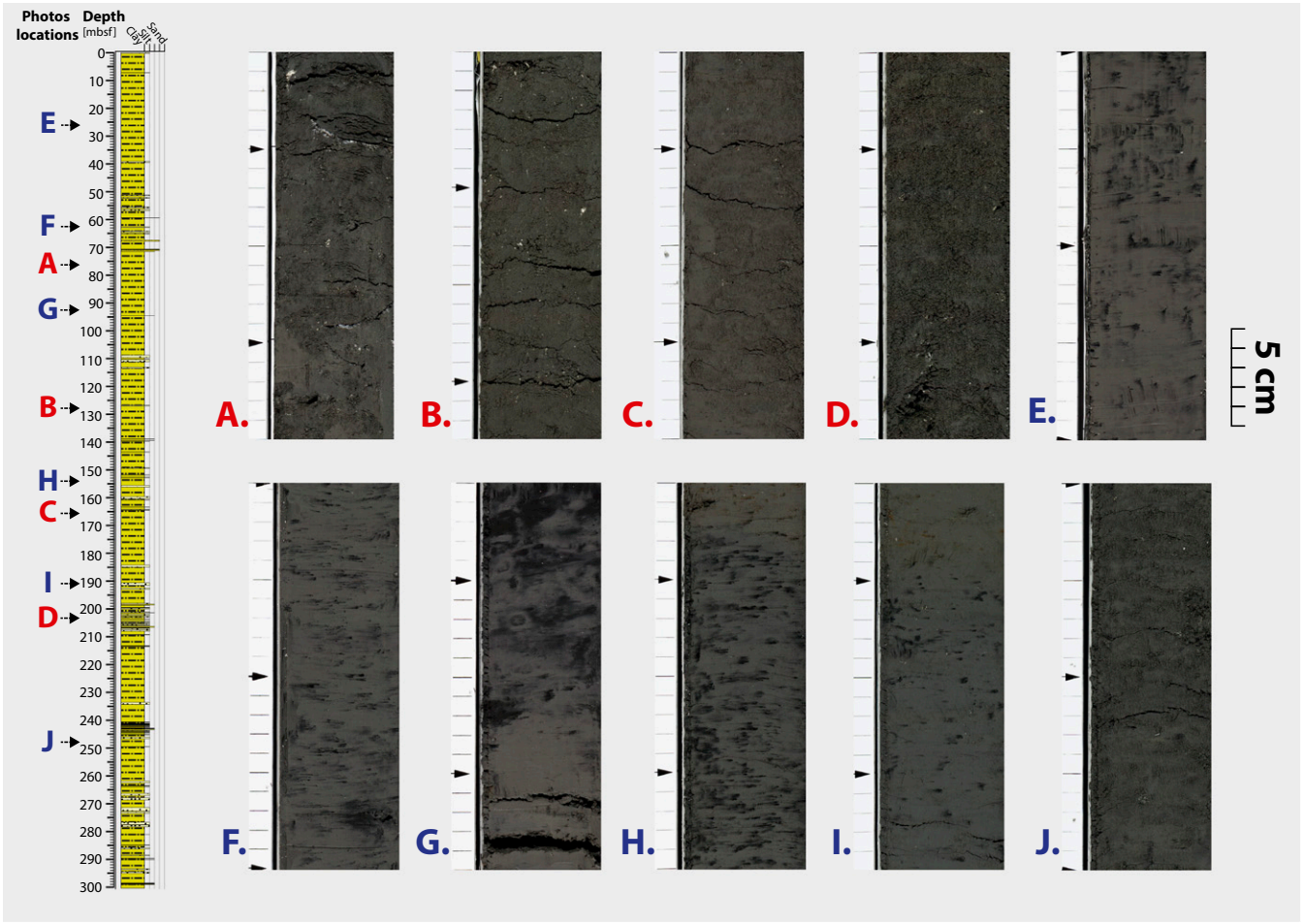

Fig. S3. Photo of selected cores. (*A*–*D*) Interglacial silty clay sedimentary facies with relatively high porosity associated with high foraminifera abundance. (*E*–*J*) Glacial sedimentation facies recorded in PRGL1-4 showing clay sedimentation with abundant organic matter spots and low porosity.

Table S1. Depth, estimated age, and associated geochemical information from samples from the PRGL1-4 borehole

PRGL1-4 depth, mbsf	Age, ky	S_{pyr}, %	$\delta^{34}S$, ‰	$\delta^{13}C$, ‰	TOC, %
Interglacial *sensu stricto*					
65.56	84.5	0.25	−41.2	−22.7	0.64
66.15	86.7	0.26	−42.0	−23.0	0.58
67.21	91.8	0.11	−42.9	−22.5	0.59
67.51	94.2	0.14	−43.4	−22.6	0.48
68.16	98.8	0.08	−37.6	−22.8	0.45
68.80	103.4	0.31	−39.7	−23.5	0.49
72.09	124.0	nd	−41.1	−23.4	0.56
72.28	127.5	0.26	−43.8	−24.3	0.63
72.32	129.3	0.10	−41.1	−23.6	0.74
72.46	130.8	nd	−41.5	−24.3	0.74
123.81	196.1	0.58	−35.9	−24.1	0.49
127.01	234.6	0.47	−41.5	−22.7	0.65
127.65	242.8	0.41	−42.8	−23.6	0.50
127.83	243.4	0.55	−43.8	−24.2	0.68
160.90	320.7	0.18	−43.2	−23.1	0.57
161.62	334.1	nd	−43.3	−24.2	0.50
161.92	336.2	0.60	−44.0	−24.8	0.75
197.29	393.5	0.27	−39.0	−24.2	0.45
198.78	401.6	0.18	−41.9	−23.4	0.35
Glacial *sensu stricto*					
8.27	18.2	0.02	−13.6	−24.6	0.69
12.50	20.2	0.05	−13.5	−24.1	0.62
15.65	21.5	0.02	−11.8	−24.5	0.58
20.19	23.6	0.53	−16.4	−24.2	0.63
23.29	25.2	0.09	−10.7	−24.5	0.58
28.09	27.8	0.17	−17.3	−24.0	0.54
32.00	31.0	0.16	−15.8	−23.9	0.51
52.10	57.4	0.24	−38.4	−22.7	0.81
52.80	58.3	0.64	−31.8	−22.7	0.74
54.17	59.9	0.37	−33.5	−23.1	0.72
54.59	60.5	0.97	−25.8	−23.3	0.68
54.96	61.0	0.14	−21.2	−23.2	0.69
55.31	61.6	0.30	−21.0	−23.2	0.67
55.51	61.8	0.20	−21.3	−23.3	0.74
56.24	62.8	0.16	−15.3	−23.3	0.73
56.61	63.4	0.10	−16.8	−23.3	0.68
57.69	63.9	0.22	−14.6	−23.6	0.59
59.46	65.3	0.24	−14.1	−23.3	0.52
60.36	66.6	0.27	−15.0	−24.0	0.53
60.68	67.1	0.19	−17.6	−24.7	0.59
61.69	68.5	0.21	−13.7	−23.7	0.52
63.51	71.2	0.11	−14.8	−23.5	0.48
64.44	75.7	0.11	−18.0	−23.4	0.50
64.89	76.6	0.26	−10.5	−24.4	0.57
78.02	135.1	nd	−27.7	−25.2	0.55
82.52	138.3	0.14	−1.6	−24.2	0.62
85.67	140.6	0.12	−9.5	−24.7	0.57
88.28	142.4	0.58	−11.4	−24.2	0.61
88.72	142.8	0.12	−7.8	−22.6	0.84
93.24	146.1	0.16	−27.1	−24.7	0.56
95.12	147.0	0.45	5.4	−24.4	0.64
97.29	147.9	0.44	−15.7	−24.0	0.64
144.97	270.0	0.17	−24.6	−24.4	0.51
146.23	271.3	0.39	−15.8	−24.6	0.53
155.49	280.4	0.06	−9.3	−24.5	0.55
166.90	340.3	0.22	−15.7	−25.3	0.55
169.05	342.0	0.58	−4.4	−25.3	0.65
170.13	342.9	0.77	10.1	−24.8	0.71
172.49	344.8	0.17	−0.7	−24.8	0.75
177.21	348.8	0.16	−19.4	−25.1	0.63
213.01	423.5	0.05	−14.6	−24.8	0.47

Table S1. Cont.

PRGL1-4 depth, mbsf	Age, ky	S_{pyr}, %	$\delta^{34}S$, ‰	$\delta^{13}C$, ‰	TOC, %
219.70	428.3	0.24	−13.8	−25.2	0.76
221.30	429.6	0.12	−10.2	−24.9	0.64
224.26	432.5	0.18	−8.7	−24.7	0.57
225.05	433.7	nd	−16.4	−25.0	0.59
226.09	435.3	0.13	−17.1	−24.6	0.62
Interglacial					
1.87	15.4	0.62	−43.5	−23.6	0.70
3.90	16.3	0.39	−42.6	−23.1	0.59
65.22	78.7	1.69	−30.2	−23.1	0.56
68.98	104.1	0.22	−32.2	−23.5	0.52
70.61	110.3	0.49	−32.0	−25.2	0.58
71.12	113.7	0.16	−32.7	−24.7	0.60
71.92	122.3	0.13	−36.4	−23.9	0.53
75.29	133.0	0.17	−31.8	−24.9	0.69
76.48	133.9	0.07	−20.9	−24.1	0.65
117.96	183.6	0.12	−38.2	−24.8	0.62
130.05	247.4	0.17	−29.9	−24.9	0.58
157.24	287.1	0.55	−36.5	−24.1	0.62
157.74	289.0	0.14	−38.8	−23.0	0.51
158.74	298.4	0.14	−37.1	−23.8	0.56
159.09	304.2	0.06	−37.7	−24.4	0.55
160.30	319.1	0.88	−1.4	−23.5	0.46
162.62	336.7	0.05	−31.6	−25.1	0.54
163.44	337.4	0.45	−34.3	−25.3	0.52
190.06	375.3	0.08	−32.4	−23.4	0.56
192.93	382.6	0.03	−18.2	−24.0	0.52
195.47	388.9	0.60	−30.3	−23.8	0.47
196.40	391.5	0.19	−9.4	−23.4	0.39
Glacial					
33.62	32.6	0.31	−25.1	−23.1	0.64
35.77	35.5	0.13	−36.1	−23.0	0.74
38.40	40.1	0.05	−27.4	−23.7	0.59
42.07	43.4	0.06	−34.7	−23.1	0.68
43.78	45.6	0.43	−17.2	−22.4	0.70
44.80	46.8	0.08	−36.3	−22.9	0.65
47.67	50.6	0.12	−35.6	−22.6	0.59
48.01	51.3	0.65	−28.8	−22.2	0.56
48.81	52.7	0.18	−34.7	−22.0	0.61
49.21	53.4	0.60	−34.5	−21.8	0.68
51.20	56.3	0.24	−22.7	−22.9	0.75
99.91	149.1	0.48	−17.3	−24.5	0.60
103.65	150.6	0.14	−26.8	−25.0	0.48
105.20	152.1	0.09	−16.3	−23.6	0.58
107.64	155.5	0.09	−28.2	−24.3	0.72
110.67	159.7	0.44	−40.2	−22.0	0.78
112.33	166.0	0.72	−34.5	−23.8	0.57
114.06	172.9	0.27	−39.0	−23.9	0.70
116.07	179.5	1.26	−24.8	−23.0	0.73
133.16	253.1	0.72	32.3	−24.7	0.56
136.45	259.2	0.47	−32.3	−23.3	0.73
140.50	265.6	0.30	−31.7	−23.2	0.60
155.89	281.7	0.10	−28.3	−23.4	0.69
156.64	284.7	0.05	−26.9	−24.2	0.55
164.51	338.3	0.20	−22.5	−25.2	0.67
181.02	353.6	0.13	−28.2	−24.7	0.53
182.99	358.0	0.12	−24.6	−24.1	0.52
184.38	361.3	0.06	−22.0	−24.7	0.52
184.41	361.5	nd	−27.6	−24.6	0.55
186.62	366.8	0.09	−15.1	−24.3	0.59
199.42	412.9	0.03	−17.6	−24.6	0.50
200.21	413.6	nd	−16.9	−25.2	0.57
206.09	418.1	0.50	18.4	−25.0	0.49

Table S1. Cont.

PRGL1-4 depth, mbsf	Age, ky	S_{pyr}, %	$\delta^{34}S$, ‰	$\delta^{13}C$, ‰	TOC, %
230.87	442.7	0.27	−34.3	−24.4	0.58
234.33	448.1	nd	−26.1	nd	nd
237.53	453.1	0.13	−14.1	−24.3	0.63
240.50	457.7	0.25	−11.6	−24.3	0.38
243.72	461.2	nd	−8.2	−24.5	0.52
243.99	461.3	0.14	−10.1	−23.9	0.48
253.29	466.3	0.05	−13.0	−24.0	0.50
267.24	473.7	0.80	−27.3	−23.7	0.50
273.68	479.0	0.19	−29.2	−22.6	0.57
273.77	479.1	0.28	−21.7	−23.8	0.53
279.50	484.7	0.36	−7.8	−24.6	0.43

Sample depths are in meters below sea floor (mbsf). Ages come from the updated age model provided in ref. 17. S_{pyr} is the weight percent of sulfur as pyrite in the bulk sediment; $\delta^{34}S_{pyr}$ and $\delta^{13}C_{org}$ are the sulfur and carbon isotopic compositions in pyrite and bulk organic matter, respectively. TOC % is the percent total organic carbon. nd indicates that the isotopic value or the abundance was not determined. Errors are given in *Materials and Methods*.